Journal of Materials Chemistry A

Crystal structure and electrical/thermal transport properties of $Li_{1-x}Sn_{2+x}P_2$ and its performance as a Li-ion battery anode material

Journal:	*Journal of Materials Chemistry A*
Manuscript ID	TA-ART-11-2020-011045.R1
Article Type:	Paper
Date Submitted by the Author:	02-Feb-2021

Complete List of Authors:	Goto, Yosuke; Tokyo Metropolitan University, Department of Physics Nakanishi, Shota; University of Hyogo Nakai, Yusuke; University of Hyogo Mito, Takeshi; University of Hyogo Miura, Akira; Hokkaido Uniuversity, Moriyoshi, Chikako; Hirosima University, Kuroiwa, Yoshihiro; Department of Physical Science, Hiroshima University, Hidetomo, Usui; Shimane University, Department of Physics and Materials Science Matsuda, Tatsuma; Tokyo Metropolitan University Aoki, Yuji; Tokyo Metropolitan University Nakacho, Yoshifumi; Moresco Corp Yamada, Yuto; Tokyo Metropolitan University, g. Department of Applied Chemistry for Environment Graduate School of Urban Environmental Sciences Kanamura, Kiyoshi; Tokyo metropolitan university, Mizuguchi, Y.; Tokyo Metropolitan University, Department of Electrical and Electronic Engineering

ARTICLE

Crystal structure and electrical/thermal transport properties of $Li_{1-x}Sn_{2+x}P_2$ and its performance as a Li-ion battery anode material†

Received 00th January 20xx,
Accepted 00th January 20xx

DOI: 10.1039/x0xx00000x

Yosuke Goto,*[a] Shota Nakanishi,[b] Yusuke Nakai,[b] Takeshi Mito,[b] Akira Miura,[c] Chikako Moriyoshi,[d] Yoshihiro Kuroiwa,[d] Hidetomo Usui,[e] Tatsuma D. Matsuda,[a] Yuji Aoki,[a] Yoshifumi Nakacho,[f] Yuto Yamada,[g] Kiyoshi Kanamura,[g] Yoshikazu Mizuguchi[a]

A new ternary layered pnictide, $Li_{1-x}Sn_{2+x}P_2$, was synthesized by a solid-state reaction and its properties were examined to explore its potential as a multifunctional material. The compound crystallizes in a layered structure in the $R\bar{3}m$ space group (No. 166) with buckled honeycomb Sn–P layers separated by mixed-occupation Li/Sn layers. Crystal structure analysis using synchrotron X-ray diffraction showed that the substitution degree of Li by Sn (x) is 0.38. Local ordering of Li/Sn occupation was demonstrated using ^{31}P nuclear magnetic resonance analysis. The thermal and electrical transport properties are significantly affected by this local ordering. The lattice thermal conductivity of $Li_{1-x}Sn_{2+x}P_2$ was found to be relatively low (1.2 $W{\cdot}m^{-1}K^{-1}$ at 525 K). The room-temperature electrical resistivity of $Li_{1-x}Sn_{2+x}P_2$ was found to be 0.3–0.4 $m\Omega{\cdot}cm$ and metallic conductivity was observed down to 0.5 K. First-principles calculations demonstrated that the electronic structure and Fermi energy of $Li_{1-x}Sn_{2+x}P_2$ are significantly dependent upon x. Moreover, the electronic structure of $Li_{1-x}Sn_{2+x}P_2$ is different from that of the related compound $NaSn_2As_2$, which shows a superconducting transition. Electrochemical measurements using a single-particle technique demonstrated the activity of $Li_{1-x}Sn_{2+x}P_2$ as an anode material for rechargeable Li-ion batteries.

1. Introduction

Solid-state chemistry is often advanced by the discovery of intriguing new functional materials. Here, materials with layered structures that show various functionalities are particularly interesting. A typical example is A_xCoO_2 (A = Li or Na). Efficient thermoelectric materials that convert directly between thermal and electrical energy,[1-5] can be achieved when A = Na because of its peculiar band shape near the Fermi level.[6,7] Interestingly, Na_xCoO_2 becomes a superconductor through hydration and Na vacancy.[8] Conversely, when A = Li ($LiCoO_2$), high-performance cathode material for Li-ion batteries, which are key components of the portable electronics, power tools, and hybrid/full electric vehicles, can be derived.[9-12] Such flexibility of characteristics is one of the main merits of layered materials that allow manipulation of their elemental compositions, electronic structures, and/or crystal structures. Thus, the development of novel layered multifunctional materials may help realize a sustainable society.

Layered tin pnictides have been investigated for a range of functionalities.[13-36] Because of the relatively weak van der Waals bonding between conducting layers (Figure 1), the production of nanometer-scale thickness sheets by exfoliation has been demonstrated for $NaSn_2As_2$ and $EuSn_2As_2$ single crystals,[13,14] providing a new platform for the study of two-dimensional materials.

Low thermal conductivity is an indispensable feature of efficient thermoelectric materials, because the efficiency of a thermoelectric module is governed by the dimensionless figure

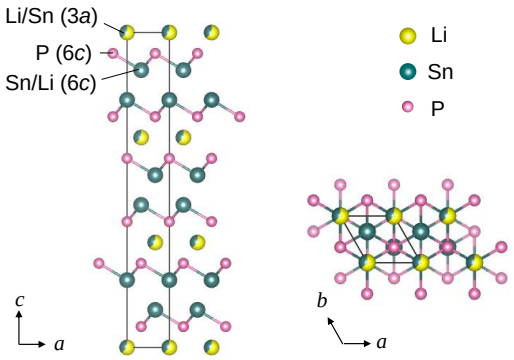

Fig. 1 Crystallographic structure of $Li_{1-x}Sn_{2+x}P_2$, showing that Li and Sn atoms exhibit mixed occupation at 3*a* site.

[a] Department of Physics, Tokyo Metropolitan University, 1-1 Minami-osawa, Hachioji, Tokyo 192-0397, Japan
[b] Graduate School of Material Science, University of Hyogo, Ako 678-1297, Japan
[c] Faculty of Engineering, Hokkaido University, Kita 13, Nishi 8 Sapporo 060-8628, Japan
[d] Graduate School of Advanced Science and Engineering, Hiroshima University, 1-3-1 Kagamiyama, Higashihiroshima, Hiroshima 739-8526, Japan
[e] Department of Physics and Materials Science, Shimane University, Matsue, 690-8504, Japan
[f] MORESCO, Minatojima-minamimachi, Chuo, Kobe, Hyogo 650-0047, Japan
[g] Department of Applied Chemistry for Environment Graduate School of Urban Environmental Sciences, Tokyo Metropolitan University, 1-1 Minami-Osawa, Hachioji, Tokyo 192-0397, Japan

†Electronic Supplementary Information (ESI) available: [details of any supplementary information available should be included here]. See DOI: 10.1039/x0xx00000x

of merit $ZT = S^2T/\rho\kappa$, where T is the absolute temperature, S is the Seebeck coefficient, ρ is the electrical resistivity, and κ is the thermal conductivity. Low lattice thermal conductivity has been demonstrated for $Li_{1-x}Sn_{2+x}As_2$ owing to its mixed-cation occupation with local ordering.[15] Furthermore, a recent study demonstrated axis-dependent carrier polarity (or goniopolarity) in $NaSn_2As_2$, indicating its potential for the construction of thermoelectric modules based on its transverse thermoelectric effect.[16] It has also been demonstrated that $NaSn_2As_2$ and $Na_{1-x}Sn_2P_2$ show superconducting transitions, meaning that these compounds can also be categorized as novel layered superconductors.[17-21]

As well as these ternary-phase materials, the binary tin phosphide Sn_4P_3 has been investigated as a rechargeable battery anode material.[22-31] For example, the high reversible capacity of 850 mA·h·g^{-1} has been achieved for a Na-ion battery with a Sn_4P_3/C composite anode.[31]

In the present study, we report the synthesis, crystal structure, and physical properties of layered $Li_{1-x}Sn_{2+x}P_2$. A polycrystalline sample was prepared by solid-state reaction. Crystal structure analysis was performed using synchrotron X-ray diffraction (SXRD), revealing mixed Li/Sn occupation, while ^{31}P nuclear magnetic resonance (NMR) analysis indicated local ordering in the mixed Li/Sn occupation, significantly affecting thermal and electrical transport properties, as demonstrated by low lattice thermal conductivity and the absence of superconductivity. We also demonstrate the activity of $Li_{1-x}Sn_{2+x}P_2$ as an anode material for Li-ion batteries using a single-particle electrochemical measurement technique.

2. Methods

Synthesis

Polycrystalline $Li_{1-x}Sn_{2+x}P_2$ was prepared by the solid-state reaction using LiP, Sn_4P_3, and Sn (Kojundo Chemical, 99.99%) as starting materials. All synthesis procedures were conducted using an Ar-filled glovebox (O_2, H_2O < 1 ppm). LiP was obtained by the reaction of Li (Kojundo Chemical, 99%) and P (Kojundo Chemical, 99.9999%) at 300−350 °C for 5 h in a sealed quartz tube. Sn_4P_3 was synthesized by a two-step solid-state reaction. A stoichiometric mixture of Sn and P was pelletized and heated at 450 °C for 16 h in a sealed quartz tube. The obtained products were powdered, pelletized, and again heated at 450 °C for 16 h in a sealed quartz tube, followed by quenching in iced water.

To prepare $Li_{1-x}Sn_{2+x}P_2$, the starting materials LiP, Sn_4P_3, and Sn were mixed at a molar Li:Sn:P ratio of 1.3:2:2 and heated at 400 °C for 20 h in a sealed quartz tube. The obtained product was densified using hot pressing at 400 °C and 50 MPa. The relative densities of the samples were all higher than 90%. The obtained samples were found to air stable, enduring at least 10 days of exposure to air without visible signs of oxidation/hydrolysis, as shown in Figure S1 in ESI.

Powder X-ray diffraction

SXRD measurements were performed at the BL02B2 beamline of SPring-8 under proposal No. 2019A1101. The diffraction data were collected using a high-resolution one-dimensional semiconductor detector (MYTHEN).[37] The wavelength of the radiation beam was determined to be 0.495813(1) Å using a CeO_2 standard. The crystal structure parameters were refined using the Rietveld method using RIETAN-FP.[38] The crystal structure was visualized using VESTA.[39] Sample morphology and chemical composition were determined using scanning electron microscopy (SEM; Hitachi TM3030) coupled with energy-dispersive X-ray spectrometry (EDX; Oxford SwiftED3000)

Nuclear magnetic resonance

^{31}P NMR analysis of a polycrystalline $Li_{1-x}Sn_{2+x}P_2$ sample was performed with a phase-coherent pulsed spectrometer (Thamway Co., Ltd.) in an 8.95 T superconducting magnet. The static ^{31}P NMR spectrum was obtained by frequency-sweep with a spin-echo pulse sequence at 295 K. Because the nuclear spin-spin relaxation times (T_2) of the two peaks were nearly identical, no T_2 correction of the NMR spectrum was performed. The ^{31}P NMR shifts were determined with reference to aqueous H_3PO_4.

Transport properties

Low-temperature electrical resistivity (ρ) was measured using the four-probe method with a physical property measurement system (PPMS; Quantum Design) equipped with a ^{3}He-probe system. ρ and the Seebeck coefficient (S) above room temperature were measured using the four-probe method and quasi-steady-state method in a He atmosphere (Advance Riko ZEM-3). The thermal conductivity (κ) was obtained using the relationship $\kappa = DC_pd$, where D, C_p, and d are the thermal diffusivity, specific heat, and sample density, respectively. The thermal diffusivity was measured by a laser flash method (TC1200-RH, Advance Riko). C_p was estimated by the Dulong–Petit model, $C_p = 3nR$, where n is the number of atoms per formula unit and R is the gas constant. d was calculated from measured dimensions and weight.

Electronic structure calculation

First-principles calculations were performed using the WIEN2k package[40,41]. Electronic structure and density of states were calculated within the generalized gradient approximation proposed by Perdew, Burke, and Ernzerhof.[42] We adopted the experimentally determined crystallographic parameters for $Li_{1-x}Sn_{2+x}P_2$. To understand the effect of the partial substitution of Li by Sn at the 3a position on the electronic band structure, we used crystal structures in which Li located at the 3a position was partially replaced by Sn and fixing the lattice constants and the internal coordinates, as shown in Figure S1 in the Supporting Information. We set a 21 × 21 × 21 k-mesh and $RK_{max} = 7$ for the calculations of the density of states and Fermi surface. We also calculated the band structure of $Li_{1-x}Sn_{2+x}P_2$ within the virtual crystal approximation using the Vienna Ab initio Simulation Package[43,44].

Table 1 Crystal structure parameters and reliability factors of $Li_{1-x}Sn_{2+x}P_2$ obtained from Rietveld refinement.[a]

Lattice system			Trigonal				
Space group			$R\bar{3}m$ (No. 166)				
Lattice parameters			a = 3.90643(5) Å				
			c = 25.3143(4) Å				
			γ = 120°				
Atom	Site	Symmetry	g	x	y	z	U (Å^2)
Li	3a	−3m	0.6248(15)	0	0	0	0.0173(6)
Sn	3a	−3m	0.3752	0	0	0	0.0173
Sn	6c	3m	1	0	0	0.21389(3)	0.01063(14)
P	6c	3m	1	0	0	0.39945(8)	0.0048(5)
R_{wp}			8.157%				
R_e			1.368%				
GOF			5.9618				

[a]Values in parentheses are standard deviations in the last digits.

Electrochemical properties

Electrochemical properties were examined using single-particle technique.[45-49] $Li_{1-x}Sn_{2+x}P_2$ powder was spread on a filter paper in an electrochemical cell. A copper-coated gold-tipped micro electrode (diameter: 10 µm) was interlocked with a manipulator (MicroSupport Quick Pro). Using an optical microscope (Keyence Corporation), the copper-coated gold tip was connected to a single $Li_{1-x}Sn_{2+x}P_2$ particle. Lithium foil was used as the counter electrode and the electrolyte was 1 M $LiClO_4$ in a mixture of ethylene carbonate (EC) and propylene carbonate (PC) (1:1, *v/v*). Electrochemical evaluation was performed with a two-electrode system. Charge and discharge tests were carried out with a galvanostat (SP-200, Bio-Logic Science Instruments Ltd) between 0.005 and 2 V (vs. Li/Li$^+$). All measurements were performed at room temperature (303 K) in an Ar-filled glovebox. Measurement of two cycles was performed with charging-discharging currents of 5 nA.

The electrochemical parameters of $Li_{1-x}Sn_{2+x}P_2$ were calculated from quasi-Tafel plots for a single particle. Quasi-Tafel plots were performed as follows:

1. Adjusting depth of discharge (DOD) by charge–discharge
2. After resting, applying the current to the particle for 5 s
3. Recording the current value and overpotential after 5 s
4. Repeating process 2 and 3 at various positive and negative current values
5. Plotting the relationship between current density and overpotential

Current densities were calculated from each current value and the surface area of the particle by assuming a truly spherical particle. In this experiment, the current values were 0.5, 0.7, 1, 2, 3, 4, 5, 7, 10, 15, and 20 nA. These were applied to both positive and negative values. This measurement was carried out for DOD 0, 25 and 75 %.

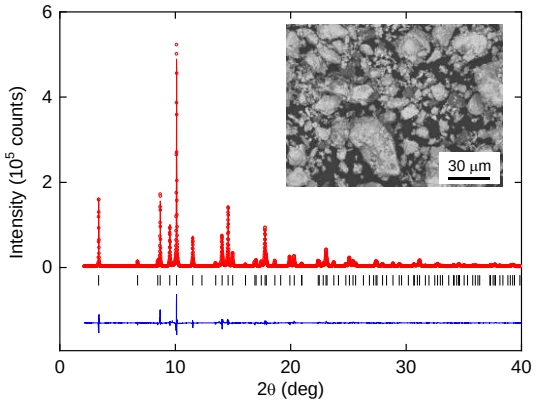

Fig. 2 SXRD pattern (λ = 0.495813(1) Å) and the results of Rietveld refinement for $Li_{1-x}Sn_{2+x}P_2$. The red circles and solid curve represent the observed and calculated patterns, respectively, and the difference between the two is shown in blue. Vertical marks indicate the calculated Bragg diffraction positions for $Li_{1-x}Sn_{2+x}P_2$. The inset shows an SEM image of $Li_{1-x}Sn_{2+x}P_2$ powder.

RESULTS AND DISCUSSION

Crystal structure analysis

Figure 2 shows the SXRD pattern of the obtained sample. All the diffraction peaks can be assigned to the trigonal $R\bar{3}m$ space group. The lattice parameters are calculated as a = 3.90643(5) Å and c = 25.3143(4) Å. These are distinctly smaller than those of isostructural $Li_{1-x}Sn_{2+x}As_2$, where a ~ 4.012(1) Å and c ~ 25.605(8) Å for x = 0.33,[15] most likely due to the lower covalent radius of P (1.10 Å) than that of As (1.19 Å).[50]

The detailed crystal structure parameters are listed in Table 1. Determination of occupancy parameters was conducted as follows: The crystal structure of $Li_{1-x}Sn_{2+x}P_2$ includes three distinct crystallographic sites: Li, 3a; Sn, 6c; and As, 6c. First, the crystal structure was refined without mixed-cation occupation, resulting in a reliability factor (R_{wp}) of 27.74%. Then, Li/Sn mixed occupation on the 3a site was allowed with two constraints:

atomic displacement parameters were set equal for Li and Sn in the same position, and the total occupancy was fixed at 100%. The refinement indicated partial occupancies of 62% Li and 38% Sn at the 3*a* position, and R_{wp} was evaluated to be 8.16%. Thus, Rietveld fitting results yielded a chemical composition of $Li_{0.62}Sn_{2.38}P_2$. Unit cell density was calculated to be 5.186 g·cm^{-3}.

In our preliminary experiments, we prepared samples using several different sets of conditions, including different temperatures and nominal stoichiometries of the starting materials. The lattice parameters of the products obtained varied from sample to sample, suggesting differing compositions for these products, as in $Li_{1-x}Sn_{2+x}As_2$.[15] However, most of these samples contain secondary phases, such as Sn_4P_3 and Sn. Accordingly, they were eliminated from further consideration in the present study.

EDX analysis showed that the Sn:P composition of $Li_{1-x}Sn_{2+x}P_2$ is 51.7(1):48.3(1), which is in reasonable agreement with that suggested by SXRD analysis. An SEM image of $Li_{1-x}Sn_{2+x}P_2$ powder is shown in the inset of Figure 2. The sample has indefinite particle shape and particles sizes ranging from micrometers to several-tens-of-micrometers in size.

^{31}P NMR

The ^{31}P NMR spectrum of $Li_{1-x}Sn_{2+x}P_2$ is shown in Figure 3(a). Because P atoms occupy a single crystallographic site as schematically shown in Figure 1, a single peak is expected in the NMR spectrum assuming that the magnetic anisotropy is not strong. However, observed spectrum shows two distinct peaks, suggesting the presence of at least two different P environments in the sample. In fact, the spectrum can be fitted well with a broader Gaussian peak at 400ppm (dashed line) and a narrower Gaussian peak at 200ppm (dotted line), where the area ratio of the two lines is 82:18.

If we assume that Sn atoms substitute into the Li (3*a*) sites randomly and with equal probability *x*, each P site may have N = 0 to 3 nearest neighboring Sn (3*a*) sites with a probability of

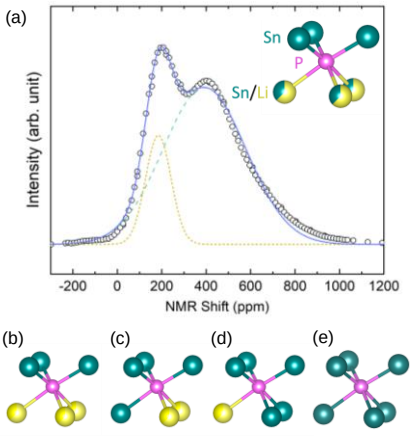

Fig. 3 (a) ^{31}P NMR spectrum of $Li_{1-x}Sn_{2+x}P_2$ recorded at 295 K. The yellow dotted and green dashed lines represent the two Gaussian functions, and the blue solid line represents their sum. Inset: Local environment around the P atoms with mixed Li/Sn occupation at the 3*a* site. (b)-(e) The local structure around the P atoms with different Sn occupancies at the 3*a* site.

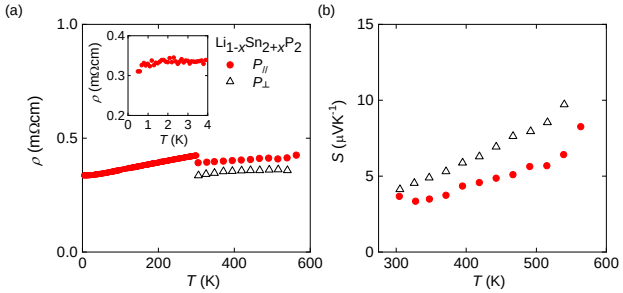

Fig. 4 (a) Temperature dependence of electrical resistivity (ρ) for $Li_{1-x}Sn_{2+x}P_2$. Above 300 K, measurement results recorded parallel ($P_{//}$) and perpendicular ($P_\perp$) to the uniaxial hot press direction are shown. (b) Temperature dependence of the Seebeck coefficient (S) for $Li_{1-x}Sn_{2+x}P_2$.

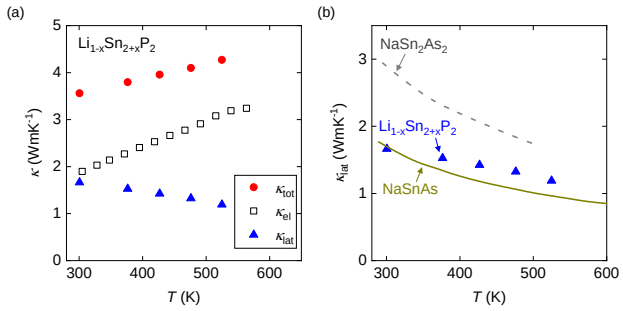

Fig. 5 (a) Temperature dependence of the total, lattice, and electronic thermal conductivities for $Li_{1-x}Sn_{2+x}P_2$. (b) Lattice thermal conductivity of $Li_{1-x}Sn_{2+x}P_2$ in comparison with those of $NaSn_2As_2$ and NaSnAs.[33]

$p(N; x) = {}_3C_N x^N(1-x)^{3-N}$. Using x = 0.38 at the 3*a* site as determined by our SXRD measurements on a same-batch sample, we estimate the probability ratio $p(N = 0; x) : [p(N = 1; x) + p(N = 2; x) + p(N = 3; x)]$ = 24:76, which is in reasonable agreement with the observed ^{31}P NMR intensity ratio (18:82). Thus, we assign the narrower peak (dotted line) as the P nucleus surrounded by 3Sn (6*c*) + 3Li (3*a*) (Fig. 3(b)) and the broader peak (dashed line) as the ^{31}P nucleus surrounded by 3Sn (6*c*) + (3−N) Li/N Sn (3*a*) (Fig. 3(c)−(e)). The broadening of the NMR lineshape at 400ppm likely arises from subtle changes in the local environment around ^{31}P nucleus due to the substitution at the 3*a* site.

Since local coordination of P with Li/Sn substitution at the 3*a* site results in a similar local structure to that of Sn_4P_3, the large ^{31}P NMR shift of Sn_4P_3 (~1000 ppm) supports our peak assignment that the larger chemical shift for the P site in which at least one of the nearest neighboring Li (3*a*) sites is substituted with Sn.[24]

In addition to the major contribution due to the random Li/Sn mixture occupancy, it should be noted that the slight deviation between the observed and calculated area ratios may be related to the presence of local ordering, as observed in the $Li_{1-x}Sn_{2+x}As_2$ system.[15]

Transport properties

Figure 4(a) shows the temperature dependence of electrical resistivity for $Li_{1-x}Sn_{2+x}P_2$. The room-temperature resistivity is around 0.3–0.4 mΩ·cm, and it decreases with decreasing temperature. No superconducting transition is observed down to 0.5 K, unlike for $Na_{1-x}Sn_2P_2$ and $NaSn_2As_2$.[17-21] The residual

resistivity ratio ρ(300 K)/ρ(0.5 K) is estimated to be 1.3, which is comparable to those of related materials.[13-15,17,18,20,21,35]

Due to the layered structure of $Li_{1-x}Sn_{2+x}P_2$, we investigated its anisotropy in resistivity with respect to uniaxial hot pressing direction above room temperature. As shown in Figure 4(a), the anisotropy in the present samples is not significant. The absolute value of the Seebeck coefficient is less than 10 $\mu V \cdot K^{-1}$, as shown in Figure 4(b). The positive sign of the Seebeck coefficient indicates that holes are the dominant carrier in the temperature region examined.

Figure 5(a) shows the temperature dependence of thermal conductivity for $Li_{1-x}Sn_{2+x}P_2$. The thermal conductivity is 3.5–4.2 $Wm^{-1} \cdot K^{-1}$ over the measured temperature range. Thermal conductivity is primarily determined by lattice and electrical contributions. The electrical thermal conductivity can be evaluated using the Wiedemann–Franz relationship, $\kappa_{el} = L\rho^{-1}T$, where L is the Lorentz number. Here, we used a degeneracy limit of $L = 2.44 \times 10^{-8}$ $V^2 \cdot K^{-2}$ to evaluate κ_{el}.

The lattice thermal conductivity was obtained by subtracting the electronic component from the total thermal conductivity. Figure 5(b) shows the calculated lattice thermal conductivity compared with those of the related materials $NaSn_2As_2$ and NaSnAs.[33] Lin *et al.* reported that lattice thermal conductivity of NaSnAs is lower than that of $NaSn_2As_2$ because of the double lone-pair electrons.[33] Although $NaSn_2As_2$ and $Li_{1-x}Sn_{2+x}P_2$ are isostructural compounds, the lattice thermal conductivity of $Li_{1-x}Sn_{2+x}P_2$ sample is lower than that of $NaSn_2As_2$ and is comparable to that of NaSnAs. This low lattice thermal conductivity is most likely because of local ordering in the mixed Li/Sn occupation for $Li_{1-x}Sn_{2+x}P_2$, as demonstrated using ^{31}P NMR (Figure 3).

It should be noted that the lattice thermal conductivity of $Li_{1-x}Sn_{2+x}As_2$ varies from sample to sample, probably due to sample dependence and/or uncertainties in the thermal conductivity measurements for very small single crystals.[15]

Electronic structure

Figure 6 shows the band structure and the Fermi surface of $Li_{1-x}Sn_{2+x}P_2$ at x = 0, 1/3, 2/3, and 1. At x = 0, the band structure and the Fermi surface are quite similar to those of $NaSn_2As_2$,[19] meaning that $Li_{1-x}Sn_{2+x}P_2$ with x = 0 could potentially exhibit superconductivity from the viewpoint of the band structure. However, the Fermi surface at x = 1/3 is totally different from that at x = 0, and the electron Fermi surface centered at the M point appears at x = 2/3 and 1. This is because the partial substitution of Li by Sn not only changes the shape of the band structure but also increases the number of electrons. The density of states for $Li_{1-x}Sn_{2+x}P_2$ is shown in Figure 7 and indicates that the Fermi energy shifts toward the energy located at the local minimum of the density of states when x increases.

It should be noted that a similar trend in the Fermi energy shift is seen within the virtual crystal approximation (as shown in Figure S3 in the Supporting Information). We thus conclude that one of the reasons that $Li_{1-x}Sn_{2+x}P_2$ does not exhibit superconductivity is the changes in the density of states and Fermi surface upon the partial substitution of Li by Sn.

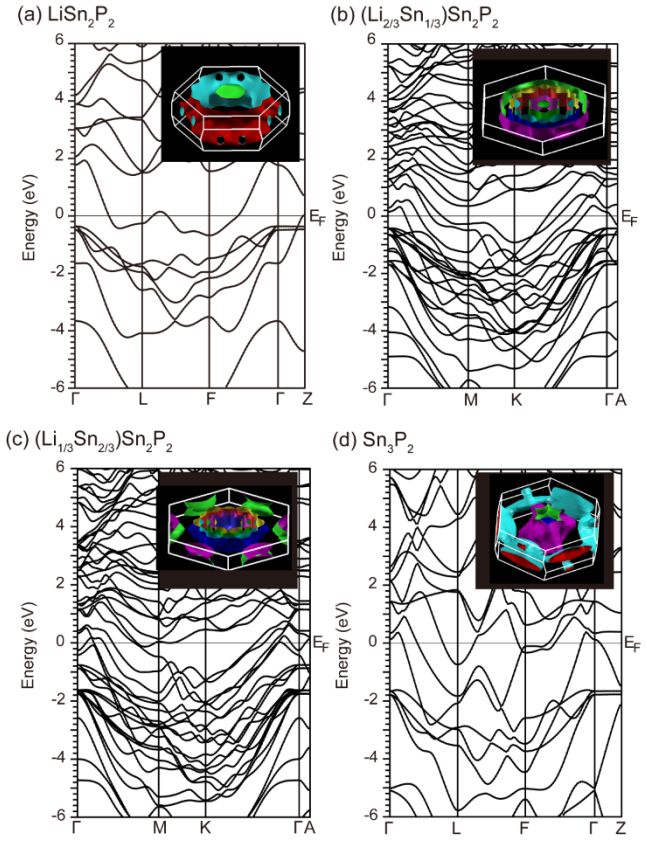

Fig. 6 Band structures of $Li_{1-x}Sn_{2+x}P_2$ for (a) x = 0, (b) x = 1/3, (c) x = 2/3, and (d) x = 1. The inset shows the Fermi surface. For calculations of x = 0 and 1, we used a primitive rhombohedral cell. For x = 1/3 and 2/3, we used a conventional hexagonal cell with $(LiSn_2P_2)_3$ as the base model. Schematic representation of the crystal structures used for the calculations is shown in Figure S2.

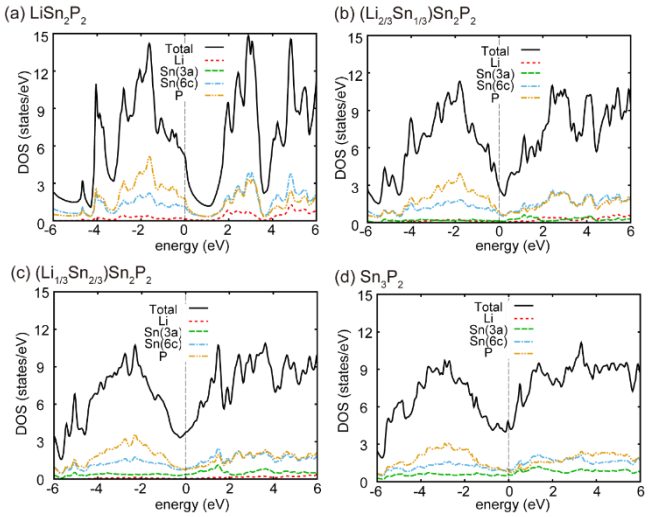

Fig. 7 Density of states for $Li_{1-x}Sn_{2+x}P_2$ for (a) x = 0, (b) x = 1/3, (c) x = 2/3, and (d) x = 1.

Electrochemical properties

Figure 8 shows the typical charge–discharge profiles of a single-particle $Li_{1-x}Sn_{2+x}P_2$ sample with a diameter of ca. 25 μm. Initial charge and discharge capacities were estimated to be ca.

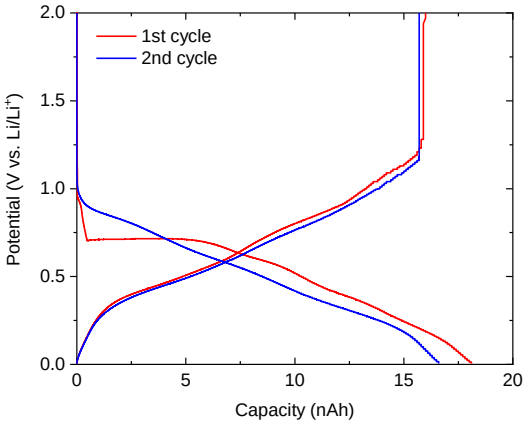

Fig. 8 Charge and discharge profiles for a single $Li_{1-x}Sn_{2+x}P_2$ particle with a diameter of approximately 25 μm.

18 and 16 nA·h, corresponding to an initial Coulombic efficiency of 88.9% at a current rate of ~ 0.3 C.

Irreversible capacity loss is observed in the first charge–discharge cycle; however, the Coulombic efficiency reaches 94% in the second charge–discharge cycle. Regrettably, the measurement probe was disconnected after the second charge–discharge cycle, probably because of the large volume change upon phase transition. Although the particle shape of $Li_{1-x}Sn_{2+x}P_2$ is indefinite (as shown in the inset of Figure 2), we assumed a spherical particle shape with diameter of 25 μm. Accordingly, the capacity of this powder was calculated at 377 $mA{\cdot}h{\cdot}g^{-1}$ using a unit cell density of 5.186 $g{\cdot}cm^{-3}$.

Figure 9 shows a quasi-Tafel plot for a single $Li_{1-x}Sn_{2+x}P_2$ particle at DOD 0%. In the small overpotential region, the kinetics of the electrochemical reaction are limited by the charge-transfer process. In this case, the plots obey the Tafel equation. In the charge region, the Tafel equation is

$$\log i = \log i_0 + \frac{\alpha F}{2.303RT}\eta$$

while in the discharge region, it is

$$\log i = \log i_0 + \frac{(1-\alpha)F}{2.303RT}(-\eta)$$

where i is current density ($mA{\cdot}cm^{-2}$), i_0 is the exchange current density ($mA{\cdot}cm^{-2}$), α is the transfer coefficient, F is the faraday constant, R is the gas constant, T is temperature (K), and η is the overpotential (V). i_0 and α values satisfying these equations could be calculated from the quasi-Tafel plots shown Figure 9.

Furthermore, the charge-transfer resistance (R_{ct}, $\Omega{\cdot}cm^2$) can be obtained from the relationship

$$R_{ct} = \frac{RT}{Fi_0}$$

In the large overpotential region, the plots deviate from the Tafel equation. This indicates that the kinetics of the electrochemical reaction are limited by Li^+ diffusion in the $Li_{1-x}Sn_{2+x}P_2$ particle. Therefore, the diffusion coefficient D ($cm^2{\cdot}s^{-1}$) in the charge and discharge process can be estimated from

$$l = \sqrt{6Dt}$$

Table 2 Kinetic parameters (exchange current density i_0, charge-transfer resistance R_{ct}, charge and discharge diffusion coefficient D_{charge} and $D_{discharge}$, transfer coefficient α of the anodic reaction) of $Li_{1-x}Sn_{2+x}P_2$ obtained at different DOD.

DOD %	0	25	75
i_0 ($mAcm^{-2}$)	0.556	0.290	0.0836
R_{ct} (Ωcm^2)	46.2	88.6	310.8
D_{charge} (cm^2s^{-1})	1.41×10^{-10}	3.83×10^{-11}	2.31×10^{-11}
$D_{discharge}$ (cm^2s^{-1})	7.76×10^{-11}	4.35×10^{-11}	1.75×10^{-11}
α	0.69	0.65	0.57

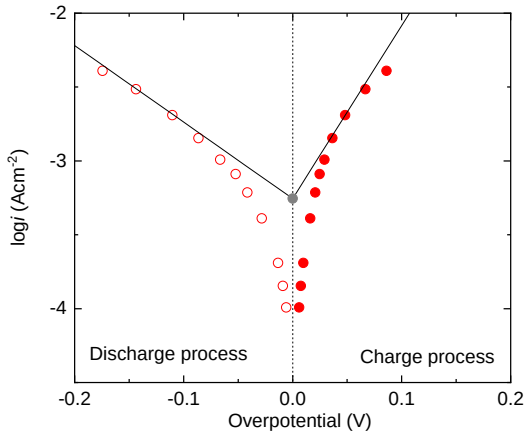

Fig. 9 Quasi-Tafel plot for a single $Li_{1-x}Sn_{2+x}P_2$ particle at DOD 0%.

where l is the particle radius (cm) and t is the charge or discharge time at the current when deviation from the Tafel equation is first observed (s).

Each electrochemical parameter at DOD = 0%, 25%, and 75% are summarized in Table 2. The electrochemical parameters obtained for $Li_{1-x}Sn_{2+x}P_2$ are comparable to those of graphite, which is most commonly used as a negative electrode material for Li-ion batteries. Therefore, $Li_{1-x}Sn_{2+x}P_2$ exhibits sufficient performance for application as a negative electrode material for Li-ion batteries.[47,51] However, it is fair to note that replacing Sn_4P_3 by $Li_{1-x}Sn_{2+x}P_2$ may not be straightforward because synthesis of $Li_{1-x}Sn_{2+x}P_2$ requires Sn_4P_3 as the precursor.

Conclusions

We presented the synthesis and characterization of $Li_{1-x}Sn_{2+x}P_2$. Its crystal structure is characterized by alternate stacking of Sn–P bilayers and mixed-occupancy Li/Sn layers. ^{31}P NMR spectral analysis revealed peak splitting, most likely due to local ordering of the Li/Sn mixed occupation. The thermal and electrical transport properties are significantly affected by this local ordering. The relatively low lattice thermal conductivity of 1.2 $W{\cdot}mK^{-1}$ is achieved at 525 K. Metallic conductivity with no superconducting transition was observed down to 0.5 K. Furthermore, an $Li_{1-x}Sn_{2+x}P_2$ particle showed suitable activity for application as a Li-ion battery anode material. The present study demonstrates that the physical properties of $Li_{1-x}Sn_{2+x}P_2$ are altered by Li/Sn mixed occupation and local ordering.

Conflicts of interest

There are no conflicts to declare.

Acknowledgements

This work was partly supported by JST CREST (No. JPMJCR16Q6), JSPS KAKENHI (No. 19K15291), and Advanced Research Program under the Human Resources Funds of Tokyo (H31-1).

Author contributions

Y. G. prepared samples and conducted thermoelectric measurements. S. N., Y. N., and T. M. carried out NMR measurements. Y. G., A. M., C. M., and Y. K performed SXRD measurements. H. U. conducted first-principles calculations. Y. G., T. M., and Y. A. carried out low temperature resistivity measurements. Y. N., Y. Y., and K. K. performed electrochemical measurements. Y. G. and Y. M. co-write the manuscript. All the authors discussed the results and commented on the manuscript

References

1 G. J. Snyder, E. S. Toberer, Complex thermoelectric materials. *Nat. Mater.* 2008, **7**, 105–114.
2 W. G. Zeier, A. Zevalkink, Z. M. Gibbs, G. Hautier, M. G. Kanatzidis, G. J. Snyder, Thinking like a chemist: intuition in thermoelectric materials. *Angew. Chem. Int. Ed.* 2016, **55**, 6826–6841.
3 L. D. Zhao, V. P. Dravid, M. G. Kanatzidis, The panoscopic approach to high performance thermoelectrics. *Energy Environ. Sci.* 2014, **7**, 251–268.
4 J. R. Sootsman, D. Y. Chung, M. G. Kanatzidis, New and old concepts in thermoelectric materials. *Angew. Chem. Int. Ed.* 2009, **48**, 8616–8639.
5 E. S. Toberer, A. Zevalkink, G. J. Snyder, Phonon engineering through crystal chemistry. *J. Mater. Chem.* 2011, **21**, 15843–15852.
6 I. Terasaki, Y. Sasago, K. Uchinokura, Large thermoelectric power in $NaCo_2O_4$ single crystals. *Phys. Rev.* 1997, **56**, R12685–R12687.
7 K. Kuroki, R. Arita, "Pudding mold" band drives large thermopower in Na_xCoO_2. *J. Phys. Soc. Jpn.* 2007, **76**, 083707–083710.
8 K. Takada, H. Sakurai, E. Takayama-Muromachi, F. Izumi, R. A. Dilanian, T. Sasaki, Superconductivity in two-dimensional CoO_2 layers. *Nature* 2003, **422**, 53–55.
9 K. Mizushima, P.C. Jones, P. J. W. and J. B. G. Li_xCoO_2 ($0 < x \leq 1$): a new cathode material for batteries of high energy density. *Mat. Res. Bull.* 1980, **15**, 783–789.
10 J. M. Tarascon, M. Armand, Issues and challenges facing rechargeable lithium batteries. *Nature* 2001, **414**, 359–367.
11 J. B. Goodenough, K. S. Park, The Li-ion rechargeable battery: a perspective. *J. Am. Chem. Soc.* 2013, **135**, 1167–1176.
12 N. Nitta, F. Wu, J. T. Lee, G. Yushin, Li-ion battery materials: present and future *Mater. Today* 2015, **18**, 252–264.
13 M. Q. Arguilla, J. Katoch, K. Krymowski, N. D. Cultrara, J. Xu, X. Xi, A. Hanks, S. Jiang, R. D. Ross, R. J. Koch, S. Ulstrup, A. Bostwick, C. Jozwiak, D. W. Mccomb, E. Rotenberg, J. Shan, W. Windl, R. K. Kawakami, J. E. Goldberger, $NaSn_2As_2$: an exfoliatable layered van der Waals Zintl phase. *ACS Nano* 2016, **10**, 9500–9508.
14 M. Q. Arguilla, N. D. Cultrara, Z. J. Baum, S. Jiang, R. D. Ross, J. E. Goldberger, $EuSn_2As_2$: an exfoliatable magnetic layered Zintl–Klemm phase. *Inorg. Chem. Front.* 2017, **2**, 378–386.
15 K. Lee, D. Kaseman, S. Sen, I. Hung, Z. Gan, B. Gerke, R. Po, M. Feygenson, J. Neuefeind, O. I. Lebedev, K. Kovnir, Intricate Short-Range Ordering and Strongly Anisotropic Transport Properties of $Li_{1-x}Sn_{2+x}As_2$. *J. Am. Chem. Soc.* 2015, **137**, 3622–3630.
16 B. He, Y. Wang, M. Q. Arguilla, N. D. Cultrara, M. R. Scudder, J. E. Goldberger, W. Windl, J. P. Heremans, The Fermi surface geometrical origin of axis-dependent conduction polarity in layered materials. *Nat. Mater.* 2019, **18**, 568–572.
17 Y. Goto, A. Yamada, T. D. Matsuda, Y. Aoki, Y. Mizuguchi, SnAs-Based Layered Superconductor $NaSn_2As_2$. *J. Phys. Soc. Jpn.* 2017, **86**, 123701–123704.
18 E. J. Cheng, J. M. Ni, F. Q. Meng, T. P. Ying, B. L. Pan, Y. Y. Huang, D. Peets, Q. H. Zhang, S. Y. Li, Nodeless superconductivity in the SnAs-based van der Waals type superconductor $NaSn_2As_2$. *EPL* 2018, **123**, 47004–47009.
19 K. Ishihara, T. Takenaka, Y. Miao, O. Tanaka, Y. Mizukami, H. Usui, K. Kuroki, M. Konczykowski, Y. Goto, Y. Mizuguchi, T. Shibauchi, Evidence for *s*-wave pairing with atomic scale disorder in the van der Waals superconductor $NaSn_2As_2$. *Phys. Rev. B* 2018, **98**, 020503–020507.
20 Y. Goto, A. Miura, C. Moriyoshi, Y. Kuroiwa, T. D. Matsuda, Y. Aoki, Y. Mizuguchi, $Na_{1-x}Sn_2P_2$ as a new member of van der Waals-type layered tin pnictide superconductors. *Sci. Rep.* 2018, **8**, 12852–12859.
21 H. Yuwen, Y. Goto, R. Jha, A. Miura, C. Moriyoshi, Y. Kuroiwa, T. D. Matsuda, Y. Aoki, Y. Mizuguchi, Enhanced superconductivity by Na doping in SnAs-based layered compound. *Jpn. J. Appl. Phys.* 2019, **58**, 083001–083006.
22 Y.-U. Kim, C. K. Lee, H. J. Sohn, T. Kang, Reaction mechanism of tin phosphide anode by mechanochemical method for lithium secondary batteries. *J. Electrochem. Soc.* 2004, **151**, A933–A937.
23 Y. U. Kim, S. Lee, C. Lee, H. J. Sohn, Enhancement of capacity and cycle-life of$Sn_{4+\delta}P_3$ ($0 \leq \delta \leq 1$) anode for lithium secondary batteries. *J. Power Sources* 2005, **141**, 163–166.
24 B. León, J. I. Corredor, J. L. Tirado, C. Pérez-vicente, On the mechanism of the electrochemical reaction of tin phosphide with lithium. *J. Electrochem. Soc.* 2006, **153**, A1829–A1834.
25 J.-J. Wu, Z. W. Fu, Pulsed-laser-deposited Sn_4P_3 electrodes for lithium-ion batteries. *J. Electrochem. Soc.* 2008, **156**, A22–A26.
26 A. Ueda, M. Nagao, A. Inoue, A. Hayashi, Y. Seino, T. Ota, M. Tatsumisago, Electrochemical performance of all-solid-state lithium batteries with Sn_4P_3 negative electrode. *J. Power Sources* 2013, **244**, 597–600.
27 H. Usui, Y. Domi, K. Fujiwara, M. Shimizu, T. Yamamoto, T. Nohira, R. Hagiwara, H. Sakaguchi, Charge–discharge properties of a Sn_4P_3 negative electrode in ionic liquid electrolyte for na-ion batteries. *ACS Energy Lett.* 2017, **2**, 1139–1143.
28 D. Lan, W. Wang, L. Shi, Y. Huang, L. Hu, Q. Li, Phase pure Sn_4P_3 nanotops by solution-liquid-solid growth for anode application in sodium ion batteries *J. Mater. Chem. A* 2017, **5**, 5791–5796.
29 H. Usui, Y. Domi, H. Nishida, K. Yamaguchi, R. Yamagami, H. Sakaguchi, *ChemistrySelect* 2018, **3**, 8462–8467.
30 W. Zhang, W. Kong, W. Zhang, W. K. Pang, V. Sencadas, Z. Guo, Z. Understanding high-energy-density Sn_4P_3 Anodes for potassium-ion batteries understanding high-energy-density Sn_4P_3 anodes for potassium-ion batteries *Joule* 2018, **2**, 1534–1547.

31 J. Choi, W. Kim, K. Kim, S. Hong, Sn_4P_3–C nanospheres as high capacitive and ultra-stable anodes for sodium ion and lithium ion batteries *J. Mater. Chem. A* 2018, **6**, 17437–17443.
32 Q. D. Gibson, L. M. Schoop, L. Muechler, L. S. Xie, M. Hirschberger, N. P. Ong, R. Car, R. J. Cava, Three-dimensional Dirac semimetals: design principles and predictions of new materials. *Phys. Rev. B* 2015, **91**, 205128–205138.
33 Z. Lin, G. Wang, C. Le, H. Zhao, N. Liu, J. Hu, L. Guo, X. Chen, Thermal conductivities in NaSnAs, NaSnP, and $NaSn_2As_2$: effect of double lone-pair electrons. *Phys. Rev. B* 2017, **95**, 165201–165207.
34 L. Y. Rong, J. Z. Ma, S. M. Nie, Z. P. Lin, Z. L. Li, B. B. Fu, L. Y. Kong, Z. Z. Zhang, Y. B. Huang, H. M. Weng, T. Qian, H. Ding, R. Z. Tai, Electronic structure of $SrSn_2As_2$ near the topological critical point. *Sci. Rep.* 2017, **7**, 6133–6138.
35 X. Gui, I. Pletikosic, H. Cao, H. J. Tien, X. Xu, R. Zhong, G. Wang, T. R. Chang, S. Jia, T. Valla, W. Xie, R. J. Cava, A new magnetic topological quantum material candidate by design. *ACS Cent. Sci.* 2019, **5**, 900–910.
36 G. M. Pugliese, F. Stramaglia, Y. Goto, K. Terashima, L. Simonelli, H. Fujiwara, A. Puri, C. Marini, M. Y. Hacisalihoglu, F. D'Acapito, T. Yokoya, T. Mizokawa, Y. Mizuguchi, N. L. Saini, Temperature dependent local atomic displacements in $NaSn_2As_2$ system. *J. Phys. Condens. Matter* 2019, **31**, 425402–425407.
37 S. Kawaguchi, M. Takemoto, K. Osaka, E. Nishibori, C. Moriyoshi, Y. Kubota, Y. Kuroiwa, K. Sugimoto, High-throughput powder diffraction measurement system consisting of multiple MYTHEN detectors at beamline BL02B2 of SPring-8. *Rev. Sci. Instrum.* 2017, **88**, 085111–085119.
38 F. Izumi, K. Momma, Three-dimensional Visualization in Powder Diffraction. *Solid State Phenom.* 2007, **130**, 15.
39 K. Momma, F. Izumi, VESTA 3 for three-dimensional visualization of crystal, volumetric and morphology data. *J. Appl. Crystallogr*. 2011, **44**, 1272-1276.
40 P. Blaha, K. Schwarz, G. K. H. Madsen, D. Kvasnicka, J. Luitz, R. Laskowski, F. Tran, L. D. Marks, WIEN2k, An Augmented Plane Wave + Local Orbitals Program for Calculating Crystal Properties (Karlheinz Schwarz, Techn. Universität Wien, Austria), 2018. ISBN 3-9501031-1-2.
41 P. Blaha, K. Schwarz, F. Tran, R. Laskowski, G. K. H. Madsen, L. D. Marks, WIEN2k: An APW+lo program for calculating the properties of solids. *J. Chem. Phys.* 2020, **152**, 074101.
42 J. P. Perdew, K. Burke, M. Ernzerhof, Generalized Gradient Approximation Made Simple. *Phys. Rev. Lett.* 1996, **77**, 3865–3868.
43 G. Kresse, J. Furthmüller, Efficient iterative schemes for ab initio total-energy calculations using a plane-wave basis set. *Phys. Rev. B* 1996, **54**, 11169–11186.
44 G. Kresse, D. Joubert, From ultrasoft pseudopotentials to the projector augmented-wave method. D. *Phys. Rev. B* 1999, **59**, 1758–1775.
45 M. Nishizawa, I. Uchida, Microelectrode-based characterization systems for advanced materials in battery and sensor applications. *Electrochim. Acta* 1999, **44**, 3629–3637.
46 K. Dokko, N. Nakata, K. Kanamura, High rate discharge capability of single particle electrode of $LiCoO_2$. *J. Power Sources* 2009, **189**, 783–785.
47 S. Lim, J. H. Kim, Y. Yamada, H. Munakata, Y. S. Lee, S. S. Kim, K. Kanamura, Improvement of rate capability by graphite foam anode for Li secondary batteries. *J. Power Sources* 2017, **355**, 164–170.
48 K. Ando, Y. Yamada, K. Nishikawa, K. Matsuda. D. Imamura, K. Kanamura, Degradation analysis of $LiNi_{0.8}Co_{0.15}Al_{0.05}O_2$ for cathode material of lithium-ion battery using single-particle measurement. *ACS Appl. Energy Mater.* 2018, **1**, 4536–4544.
49 N. Umirov, Y. Yamada, H. Munakata, S. S. Kim, K. Kanamura, Analysis of intrinsic properties of $Li_4Ti_5O_{12}$ using single-particle technique. *J. Electroanal. Chem.* 2019, **855**, 113514–113520.
50 Emsley, J. The Elements, 3rd ed.; Clarendon Press: Oxford, U.K., 1998.
51 M. N. Obrovac, V. L. Chevrier, Alloy negative electrodes for Li-ion batteries. *Chem. Rev.* 2014, **114**, 11444–11502.

